International Journal of Fatigue 149 (2021) 106268

Contents lists available at ScienceDirect

International Journal of Fatigue

journal homepage: www.elsevier.com/locate/ijfatigue

Influence of deposition strategies on tensile and fatigue properties in a wire + arc additive manufactured Ti-6Al-4V

Abdul Khadar Syed [a,*], Xiang Zhang [a], Armando Caballero [b], Muhammad Shamir [a], Stewart Williams [b]

[a] Faculty of Engineering, Environment and Computing, Coventry University, Coventry CV1 5FB, UK
[b] Welding Engineering and Laser Processing Centre, Cranfield University, Cranfield MK43 0AL, UK

ARTICLE INFO

Keywords:
Additive manufacturing
WAAM
Titanium alloys
Tensile
Fatigue

ABSTRACT

This paper investigates the influence of two different deposition strategies, oscillation and parallel pass, on the tensile and high cycle fatigue properties of a wire + arc additive manufactured Ti-6Al-4V alloy in the as-built condition. In the oscillation build, the plasma torch and the wire feeder continuously oscillated across the wall thickness direction. In contrast, four single layers were deposited consecutively in the same direction along the wall length in the parallel pass build. Test specimens were manufactured in horizontal and vertical orientation with respect to the deposited layers. Compared with the parallel pass build, the oscillation build had lower static strength due to its coarser transformation microstructure. However, the elongation values were similar. The presence of columnar primary β grains has resulted in anisotropic elongation values. The vertical samples with loading axis parallel to the primary β grains showed 40% higher elongation than the horizontal samples. The fatigue strength was comparable with its wrought counterpart and greater than typical material by casting. At 10^7 cycles, fatigue strength of 600 MPa was achieved for the oscillation build vertical samples and the parallel pass build in both orientations. Only the oscillation build horizontal samples had lower fatigue strength of 500 MPa. Fractography analysis showed that most of the samples (about 70%) had crack initiation from pores, about 20% samples had crack initiated from microstructural features and the rest did not failed (runouts at 10^7 cycles).

1. Introduction

Although Additive Manufacturing (AM) offers new avenues to produce near net-shaped parts with design flexibility and raw materials savings, one of the main challenges for industrial adoption of AM is the uncertainty and variability in mechanical properties and structural performance [1]. This uncertainty arises due to the AM process inherent microstructure and defects. Titanium alloy Ti-6Al-4V (Ti64 hereafter) is one of the most researched materials by AM due to its high manufacturing cost by traditional manufacturing processes and its excellent combination of mechanical properties and widespread applications in various industries such as the aerospace, energy, nuclear and biomedical [2,3]. In general, AM built Ti64 consists of columnar primary β grains oriented along the build direction. As a result, material property anisotropy has been observed. The tensile strength of Ti64 built by Laser Powder Bed Fusion (LPBF) is generally above the specification recommended for powder bed fusion AM process in ASTM F2924 standard [4]. In the as-built condition, the presence of columnar primary β grains caused marginal anisotropy in static strength values; the horizontal samples (loading axis normal to the material build direction) showed higher tensile and yield strength than that of the vertical samples (loading axis parallel to the build direction) [5–7]. However, a mixed behaviour of ductility was found. Vertical samples showed 50% higher ductility in [5], whereas the horizontal samples showed 30% higher ductility in [6]. In contrast, no anisotropy in ductility was found in [7]. The inconsistency in the ductility is due to the presence of a large number of process inherent gas pores and lack of fusion defects which acted as damage initiation sites [5–7]. An Electron Beam Melted (EBM) Ti64 showed lower yield and tensile strength by 25% and 30% respectively, and higher ductility by 75% compared to the LPBF Ti64 [2]. This was owing to the pre-heating of the powder and, therefore, slower cooling rates in the EBM process resulting in a fully transformed coarser transformation microstructure compared to LPBF [2,8]. Ti64 built by powder feed laser directed energy deposition AM process showed

* Corresponding author.
E-mail address: abdul.syed@coventry.ac.uk (A.K. Syed).

https://doi.org/10.1016/j.ijfatigue.2021.106268
Received 15 February 2021; Received in revised form 24 March 2021; Accepted 4 April 2021
Available online 15 April 2021
0142-1123/© 2021 The Authors. Published by Elsevier Ltd. This is an open access article under the CC BY license (http://creativecommons.org/licenses/by/4.0/).

similar strength properties as EBM Ti64, but the ductility was 30% lower [2,9,10].

Wire + Arc Additive Manufacturing (WAAM) is a directed energy deposition AM process using wire as raw material and a plasma arc as an energy source [11]. Similar to other AM processes, microstructure directionality is found in WAAM Ti64 due to the large heat input and thicker layer deposition [12]. The average yield and tensile strength of WAAM Ti64 built by single pass deposition are 10% lower than forged Ti64 bar with a similar ductility [12]. The presence of columnar grains resulted in anisotropic tensile properties in WAAM Ti64, where the horizontally oriented samples showed higher tensile strength and lower ductility than vertically orientated samples [12]. Several studies have successfully applied in-situ deformation (cold working) by rolling [13–16] and machine hammer peening [17,18] during the WAAM process to refine the primary β grains. The large strain introduced in the previously deposited layer helped to reduce the peak tensile residual stresses and the deformation in a straight AM wall [13]. Furthermore, it has reduced the primary β grain size and weakened its crystallographic texture [13–16]. The yield and tensile strengths were increased after cold working. This is due to recrystallisation resulting from the deformation process, which has also reduced the α lath width and its crystallographic texture [15][19]. However, the ductility after cold working was lowered due to the increased number of grain boundaries, which will facilitate a weaker path for failure, but it is still comparable with wrought material [19]. Similarly, hammer peening also resulted in increased yield and tensile strength compared to without hammer penning. Although the ductility was decreased to 11% after hammer peening, it is still above the ductility (i.e. 10%) of the Wrought AMS 4928 standard [20].

Changing the cooling rate by extracting heat from the build plate [21] and active inter-pass cooling using compressed CO_2 [22,23] has shown a marginal improvement in the tensile strength. However, the ductility was considerably reduced owing to acicular α formation as a result of the increased cooling rate [22,23]. Post deposition heat treatments are successfully applied on WAAM built Ti64 to refine the grain size, which increased the tensile strength by around 12% with the expense of a 30% reduction in ductility [24]. Bermingham et al. [25] attempted to eliminate the deleterious anisotropic microstructure in WAAM Ti64 by adding trace boron levels. The addition of boron helped to restrict the columnar grain growth by constitutional supercooling and promoted nucleation and growth of neighboring grains [25]. In the as-deposited condition, the addition of boron did not influence strength but improved ductility. However, post-deposition heat treatment of Ti64 with boron addition offered a 10% greater strength and 40% improvement in ductility compared to unmodified Ti64 [25].

In terms of fatigue performance, limited research is carried on WAAM Ti64. Samples produced by the single-pass deposition strategy were tested by Wang et al. at the maximum applied stress 600 MPa and cyclic stress ratio of 0.1 in two sample orientations, i.e. loading axis either parallel or perpendicular to deposited layers [12]. The fatigue life was found to be 10% higher than that of a wrought mill annealed counterpart [12]. However, a small number of samples failed prematurely due to crack initiation from gas porosity defects formed as the result of wire contamination during the deposition. It should be stated that WAAM Ti64 seldom generates pores or other types of defects; the material usually being fully dense [19,33]. Biswal et al. [26] investigated the change in morphology of purposely built gas pores in WAAM Ti64 under cyclic loading via X-ray computed tomography (XCT) and found that the pores doubled their size after subjecting to fatigue loading. This has resulted in a 65–85% reduction in the specimen's total fatigue life [26]. In another study [27], the effect of purposely introduced porosity defects on the fatigue performance of WAAM Ti64 built by the oscillation build strategy and tested with the loading axis perpendicular to the deposited layers was studied. The fatigue strength of samples without defects was comparable to its wrought counterpart. Neverthless, the fatigue strength was reduced by about 8% in WAAM samples with defect diameter smaller than 100 μm and further reduced by around 40% when defect diameter was larger than 100 μm. The large scatter found in the test data was thought of owing to the defect location [27]. A recent follow-up study showed that variations in the local microstructure and its crystallographic orientation around the defect had played an important role in fatigue data dispersion. For the same applied stress, samples had longer fatigue life if they had smaller grain size and higher distribution of the Schmid factor (described the slip plane and slip direction which resolves the most shear stress in stressed material) for the pyramidal slip system around the defect [28].

Using the single-pass build method, where a single bead is deposited layer by layer fashion, material thickness is limited to 10 mm. New deposition strategies, i.e. oscillation and parallel pass, have recently been developed for the WAAM process to increase the deposition rate and produce parts with greater, and variable, wall thickness [29,30]. For the oscillation build, the plasma torch and the wire feeder were continuously oscillated across the wall thickness direction, with an approximate 50% overlap between the melt tracks as the process head was progressively translated along the wall length direction. In the parallel pass build, four parallel passes were deposited in each layer that are aligned with the wall length. The four parallel passes have a 50% overlap between each pass. For each track, the process head was translated in the same direction along the wall. So far, the fatigue performance of WAAM Ti64 was partially investigated in the single pass [12] and oscillation build strategies [27]. In [12], samples with a loading axis either parallel or perpendicular to deposited layers was tested only at 600 MPa applied stress, whereas only oscillation build samples with loading axis perpendicular to deposited layers was tested in [27]. Since new deposition strategies have considerable influence on the cooling rate, a systematic study on the influence of two different deposition strategies on the microstructure, tensile and fatigue properties in WAAM Ti64 is necessary to support the durability design. Samples were tested in the as-built condition with the loading axis either parallel or perpendicular to the deposited layers to understand the influence of columnar primary β grain on the mechanical property anisotropy. The results are compared with traditional wrought and cast counterparts and discussed in the context of microstructural analysis and various crack initiation sources.

2. Materials and methods

WAAM Ti64 walls were deposited using a Fronius Plasma 10 module attached to a rotator, allowing the co-axial rotation of the shield, wire feeder and the wire spool around the plasma torch. Deposition was built on a 12 mm thick hot-rolled Ti64 plate that was clamped to a rigid steel backing plate to minimise the distortion due to thermal residual stresses. A plasma arc was used as the energy source and a 1.2 mm diameter wire of AWS 5.16- grade-5 Ti64 as a feedstock. The chemical composition of the wire was taken from the product certificate, which is as follows (wt-%): Al = 6.24, V = 4.18, Fe = 0.13, O = 0.15, C = 0.013, N = 0.009, H = 0.005, and balance Ti. An argon gas of 99.99% purity was used to create an inert atmosphere within the welding tent. The oxygen content in the tent was monitored and was generally between 200 and 600 ppm. The process parameters were travel speed 5.5 mm/s, wire feed rate 2.2 m/min, arc voltage, 20 V, and arc current 160 A.

Two build strategies were used, oscillation and parallel pass, Fig. 1a-b. During the oscillation build, the plasma torch and the wire feeder have continuously oscillated across the wall thickness direction (TD)

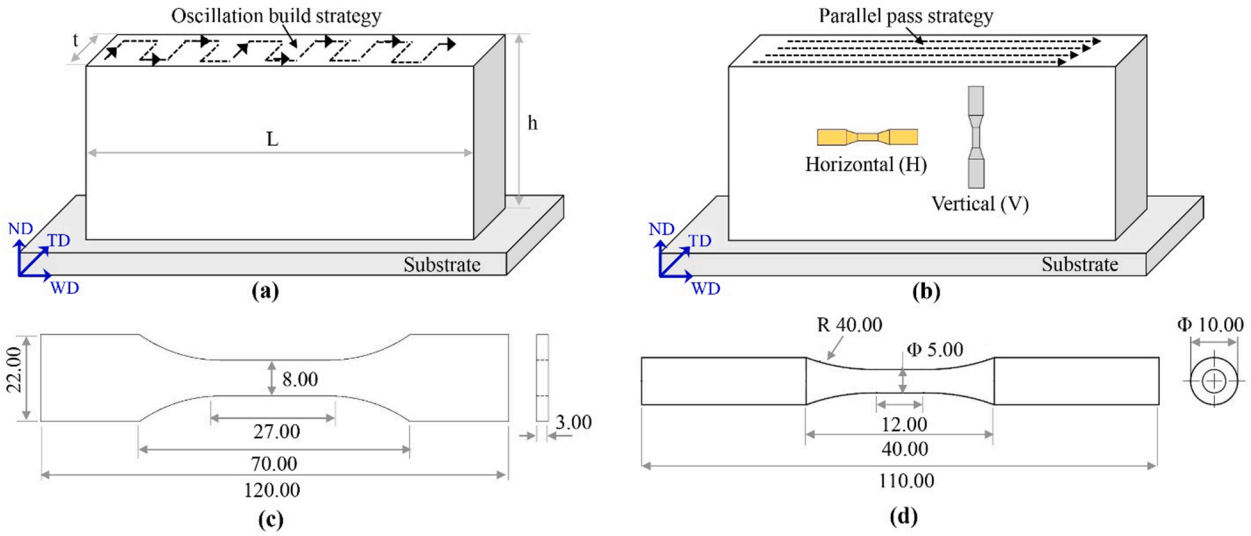

Fig. 1. Schematic of Ti64 walls showing oscillation (a) and parallel pass (b) deposition strategies, and sample orientations. WD = heat source travel direction, TD = wall transverse or thickness direction, ND = build height direction. Geometry and dimensions of tensile (c) and fatigue (d) samples. Unit: mm, not to scale.

with about 50% overlap between the melt tracks. For parallel pass build, four single parallel layers were deposited consecutively in the same direction along the wall length with a 50% overlap between adjacent passes along the heat source travel direction (parallel to the wall WD direction). One wall was deposited for each build strategy with dimensions in length (L) × height (h) × thickness (t) of; 440 × 140 × 22 mm. After the material deposition, the wall was removed from the base plate and used to extract tensile and fatigue samples by electric discharge machining.

Tensile and high cycle fatigue (HCF) test samples are distinguished as either "horizontal" or "vertical", as defined in Fig. 1b. In the horizontal orientation, the loading axis is parallel to the deposited layers (on WD-TD plane and perpendicular to columnar β grains), whereas the loading axis is perpendicular to the deposited layers (along ND-TD plane and parallel to columnar β grains) in vertical samples. The geometry and dimension of tensile and fatigue samples are presented in Fig. 1c-d, respectively. The testing was carried at room temperature. Tensile test samples were designed according to the ASTM E8 standard [31]. Five tensile tests each in the horizontal and vertical orientation were performed using a 100 kN servo-hydraulic test machine. The test was performed with a displacement rate of 1 mm/min, and the strain was measured with a 25 mm gauge length extensometer. The average yield strength (YS), ultimate tensile strength (UTS) and elongation were determined from the recorded tensile test data.

Fatigue samples were designed and tested according to ASTM E466 standard [32]. The sample gauge section was polished using 4000 grit SiC papers to reduce the average maximum surface roughness of 0.2 μm along the loading direction as specified in [32]. Load controlled fatigue testing was carried out at room temperature on 100 kN servo-hydraulic test machine under constant amplitude sinusoidal wave loading with a load ratio of $R = P_{min}/P_{max} = 0.1$, at 50 Hz frequency. After failure, all the samples are analysed under a scanning electron microscope (SEM) to identify the crack initiation sources and fracture mechanisms.

For microstructure analysis, an optical light microscope and SEM were used. Primary β grain and the α lath width measurements were carried out on images taken from the center of the cross-section samples extracted from the WD-ND plane. The linear intercept method described in ASTM E1382 standard [33] was used to measure the grain size. For primary β grain widths measurements, five images were taken using an optical microscope and the length of the intercepts across each line was determined using the Image-J software. Five high resolution SEM images were taken at different locations along the build direction to take into account the strong anisotropy in the microstructure. The α lath width was determined by $\frac{1}{1.5(1/\lambda)_{mean}}$, where λ_{mean} is the mean intercept length.

3. Results and discussion

3.1. Microstructure analysis

Photographs of large-scale microstructural features are presented in Fig. 2a-b. The layer-wise deposition with large layer increments (thicker layer deposition) and local thermal history in the WAAM process has resulted in white layer bands spaced equally along the build direction. These microstructural bands correspond to Heat Affected Zones (HAZ) produced by the thermal gradient generated by translated heat source [34]. HAZ bands appear as a regularly spaced horizontal line in the oscillation build and parallel pass build WD-ND plane, whereas a 'fishy scale'-like curved pattern can be seen in the parallel pass build TD-ND plane. HAZ bands are not present at the top of the oscillation build, whereas parallel pass build shows HAZ bands along the entire height of the wall, refer to the TD-ND plane photographs in Fig. 2a-b. Curved HAZ bands in the parallel pass deposit (Fig. 2b, TD-ND plane) are formed as the result of four single parallel layers deposited consecutively across the wall width, which were deposited with a 50% overlap between passes along the heat source travel direction (TD-ND plane) parallel to the wall WD direction. The four single passes have resulted in four curved HAZ bands in the parallel pass deposition. On the other hand, although the oscillation build has a 50% overlap between the oscillations along the TD plane, it did not result in curved HAZ bands (Fig. 2a, WD-ND plane) as observed in the parallel pass build (Fig. 2b, TD-ND plane). A detailed investigation of HAZ bands in WAAM Ti64 was studied in [35]. According to [35], HAZ bands in WAAM are caused by re-heating the previously deposited layer where the temperature reaches just below the β transus temperature during the subsequent layer deposition. Such continuous thermal cycles lead to coarsening of the lamellar transformation structure within the HAZ bands and the formation of a thin layer with a finer α lamellar single variant colony microstructure just below the β transus (~990 °C) [36]. Similar HAZ bands have also been

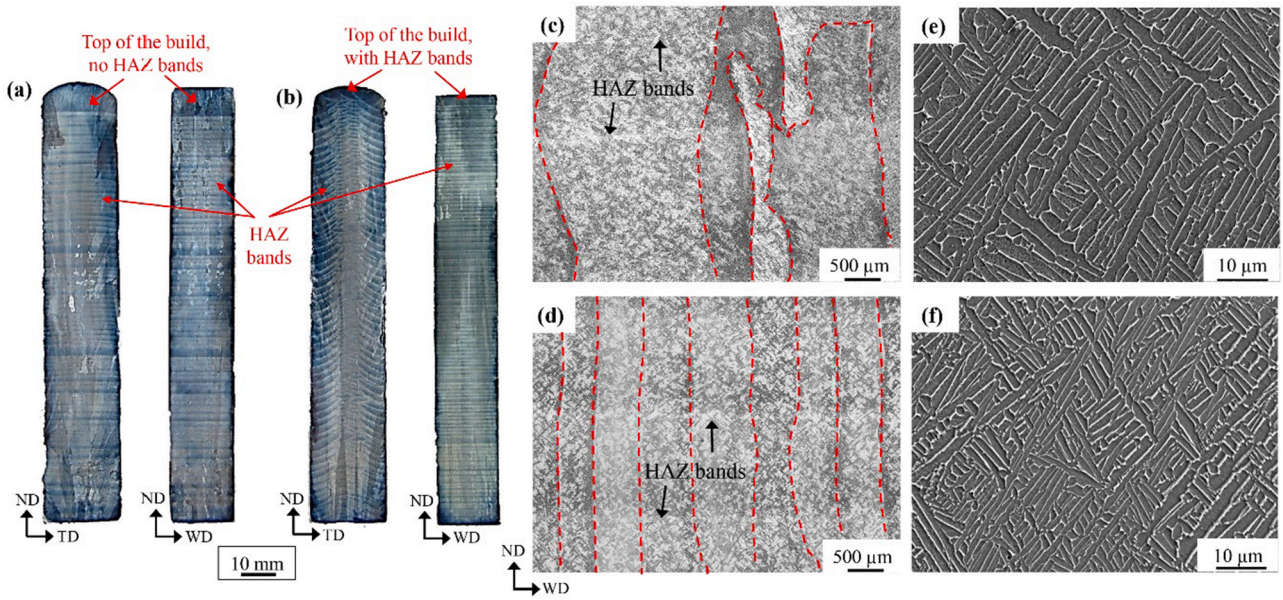

Fig. 2. Large scale photographs of TD-ND and WD-ND planes showing white layer bands along the build (a) oscillation build, (b) parallel pass build. Lower magnification optical micrographs of WD-ND plane for (c) oscillation build, (d) parallel pass build showing columnar primary β-grains (delineated for better visualization). Higher magnification of SEM micrographs of (e) oscillation and (f) parallel pass build.

reported in other wire feed [37], powder feed [36] and powder bed [38] AM processes.

The WD-ND plane lower magnification optical micrographs of oscillation and parallel pass builds are presented in Fig. 2c-d. In both builds, coarse columnar primary β grains grow along the deposited layers aligning close to the build direction (ND). This is the direct consequence of the steep thermal gradient at the solidification front in a heated melt pool and low solute portioning in this alloy [14,15,39]. During the deposition, reheating the previously deposited layers by the plasma arc causes reheating above the β transus and remelting, depending on the distance from the heat source. This allows the residual β to re-form the primary β grain structure produced in the previous deposition track below the new fusion boundary. When combined with the low constitutional supercooling of Ti64, this results in solidification primarily by epitaxial growth from the grains that re-form at the fusion boundary, and large columnar beta grains can then develop through multiple deposition layers [40]. The macrostructure in AM Ti64 is sensitive to the processing conditions. This is evident by the size of the β grains presented in Fig. 2c-d. The primary β grains are much wider (although narrower β grains are also observed occasionally), with a width ranging between 0.4 and 3.2 mm and an average width of 1.63 ± 0.58. On the other hand, the parallel pass build has narrower primary β grains with a width ranging between 0.1 and 0.7 mm with an average width of 0.37 ± 0.15. In the oscillation build, the heat source travels along the WD direction and oscillates along the TD, whereas the parallel pass build is deposited along the WD without any oscillation. This has influenced the local thermal conditions during the oscillation build resulting in wider primary β grains.

Fig. 2e-2f show higher magnification SEM micrographs of the typical transformation microstructure between two HAZ bands of oscillation and parallel pass builds. Classical α + β microstructures with both basketweave and colony morphologies can be seen. Measured average α lath width is 2.27 ± 0.12 µm for oscillation build, and 0.93 ± 0.15 µm for parallel pass build. The oscillation build showed large α colonies compared to the parallel pass build. The coarser transformation microstructure in the oscillation build is due to a much slower cooling rate through the β-transus compared to the parallel build. With the oscillation build, there is a much shorter delay time between overlapping tracks when oscillating the heat source across the wall width, compared to when using repeated parallel passes along the wall length in parallel build. Therefore, the oscillation build strategy had a more dramatic effect on reducing the cooling rate through the β to β + α transformation and consequently produced the coarsest transformation microstructure of the two build strategies.

3.2. Tensile properties

Fig. 3 shows one of the stress–strain curves from five test samples in each orientation for oscillation and parallel pass builds. Table 1 shows the average values of mechanical properties and the standard deviation deduced from five tests in each sample orientation. Between the two build strategies, oscillation build showed marginally lower yield and tensile strength. The measured α lath width in the oscillation build is approximately 2.5 times larger than the parallel pass build. The smaller α lath width delays onset of plastic deformation, hence a higher yield

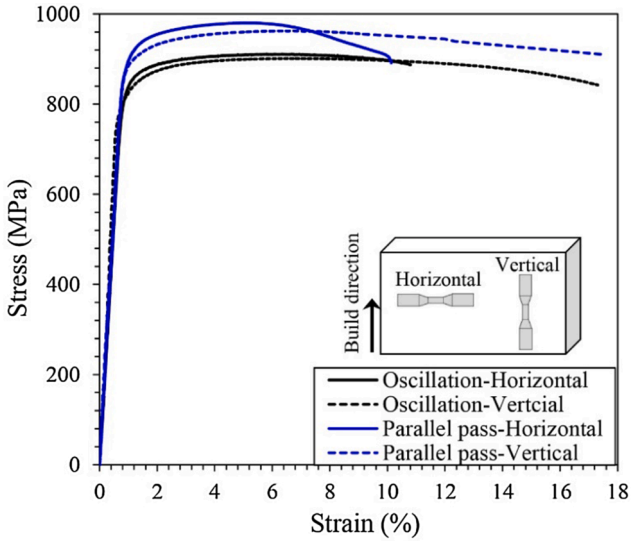

Fig. 3. Average tensile test curves for oscillation and parallel pass build samples.

Table 1
Tensile properties of two build strategies in two sample orientations and comparison with conventional manufactured wrought [20] and cast [20] counterparts and minimum tensile properties recommended for AM Ti64 in [4].

Material property	Oscillation build		Parallel build		Wrought (AMS 4928)	Cast (AMS 4992)	ASTM F2924
	Horizontal	Vertical	Horizontal	Vertical			
Yield strength (YS), MPa	842 ± 14	800 ± 23	900 ± 18	872 ± 16	861	765	825
Ultimate tensile strength (UTS), MPa	951 ± 12	898 ± 24	981 ± 13	952 ± 9	930	861	895
Elongation (%)	11 ± 2	17.3 ± 5	10.5 ± 3	17.5 ± 4	25	5	10

and tensile strength were observed in parallel pass build. The influence of sample orientation is clearly shown on the ductility. An average strain to failure of 11% and 17% was recorded for the horizontal and vertical samples respectively showing the influence of sample orientation on ductility. The mechanism for the anisotropy in ductility between the horizontal and vertical samples in this study is directly related to the anisotropic microstructure found in both builds. The tensile loading axis in the horizontal samples is normal to the primary β columnar grains and α_{GB}. It is well documented that α_{GB} normal to the loading direction furnishes as a preferential path for local strain accumulation along the grain boundary, thereby damage initiation which separates the adjacent primary β grains leading to lower ductility [10]. Therefore, much lower ductility was measured in the horizontal samples of both build strategies. Conversely, tensile loading in the vertical samples is parallel to the primary β grains and α_{GB} where the bulk microstructure also contributed to the plastic deformation, thereby increasing ductility in the vertical samples [10].

WAAM Ti64 tensile properties are compared with conventional manufactured Ti64, i.e. AMS 4928 wrought bar, annealed (12.7 mm thickness), casting, HIPed and annealed (less than 12.7 mm thickness) and ASTM F2924. WAAM Ti64 tensile strengths are comparable with conventional wrought and considerably higher than the cast materials and minimum tensile properties requirements by ASTM F2924 for AM built Ti64. Comparing to the wrought, WAAM Ti64 ductility is 55% lower in horizontal samples and 30% lower in vertical samples in both the build strategies. Compared with the cast, horizontal and vertical samples from both the build strategies showed 2 × and 3.5 × higher ductility respectively. α lath width and α colony size greatly influence the plastic deformation, i.e. smaller α lath width and α colony size delay the onset of the plastic deformation [41,42]. The α lath width measured in WAAM Ti64 is significantly lower than the wrought and cast; hence, overall, better tensile and yield strength is observed.

3.3. Fatigue behaviour

High cycle fatigue (HCF) test results for the oscillation and parallel pass builds in two sample orientations are presented in Fig. 4. Fatigue data for the mill annealed wrought sheet (2 mm thick, L-T orientation) and cast plate (12.7 mm thick) are also presented in the same figure. Fatigue strength of the WAAM specimens was higher than the cast material and only marginally lower than the wrought, except the oscillation build horizontal samples tested at 500 MPa.

In defect-free material, crack initiation is associated with the localisation of cyclic slip. In Ti64 subjected to cyclic loading, the α phase and α_{GB} hinder plastic slip localisation, thereby resulting in improved fatigue performance. In general, the finer the α phase, the more resistance there is for cyclic slip and the higher the crack initiation resistance. The wrought Ti64 have a bimodal microstructure and have higher crack initiation resistance and good HCF performance [43]. In comparison, early crack initiation from casting defects and fully lamellar microstructure in cast material leads to lower HCF performance [44]. On the other hand, WAAM Ti64 has a fine basketweave colony microstructure provides greater crack initiation resistance than the cast and is only marginally lower than wrought material. WAAM Ti64 samples in both build strategies are dominated by columnar grains, which has resulted in anisotropy in the elongation (higher elongation in vertical samples). Of the two deposition strategies, the parallel pass build shows a marginally higher fatigue life than the oscillation build (refer Fig. 5). In Ti64, resistance to crack initiation in the HCF regime is dependent primarily on the α lath width and α colony size, which influence resistance to dislocation motion, thereby cyclic slip length [45]. Previous studies have demonstrated that, an increased α lath width would cause decreased fatigue life [45]. The parallel pass build has finer α laths (0.93 μm) compared to the oscillation build (2.27 μm); hence observed a marginally higher fatigue performance.

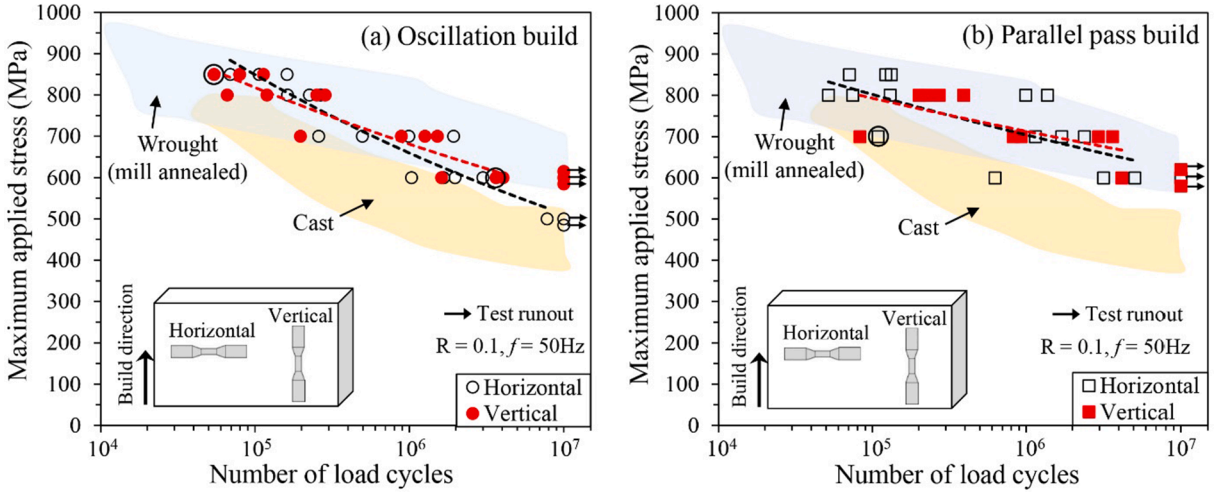

Fig. 4. Maximum applied stress vs load cycles (S-N curves) for oscillation and parallel pass build strategies Encircled data points indicate crack initiation from a surface pore. Best fitted lines are drawn. Conventional manufactured Ti64 wrought [20] and cast [20] are also shown.

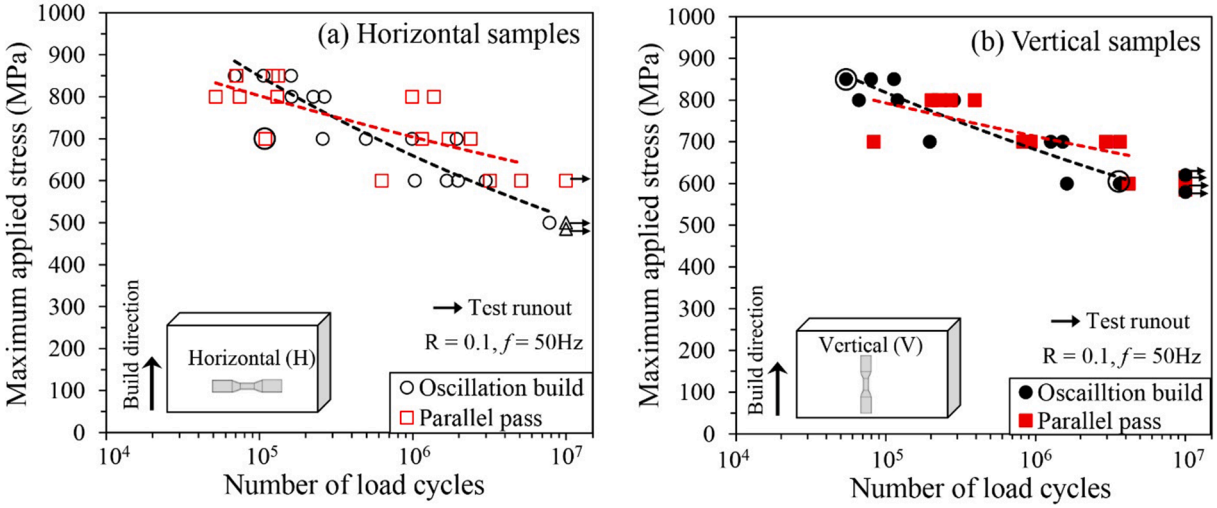

Fig. 5. A comparison of S-N data along with the best fit curves (dashed lines) for both build methods in horizontal and vertical orientation. Encircled data points indicate crack initiation from a surface pore.

The influence of sample orientation on fatigue life can also be seen in Fig. 4. A mild anisotropic behaviour is found only in the oscillation build where at 10^7 cycles, the vertical samples showed higher fatigue limit strength of 600 MPa than the horizontal samples (500 MPa). On the other hand, there is virtually no difference in the fatigue limit between the parallel pass build's horizontal and vertical samples. S-N data comparison of horizontal and vertical samples of both build methods are presented in Fig. 5. It can be noticed that the fatigue life of horizontal samples in both build methods is similar when the applied maximum stress is $\geq$ 700 MPa. From the β grain width measurements presented in section 3.1, we can see that a smaller number of β grains per unit volume are present in the oscillation build compared to a parallel pass. A lower number of β grains per unit volume cause a low misorientation between them, thus produce a limited number of α variants, which gives a strong α texture [15]. Whereas a higher number of β grains per unit volume leads to high misorientations, producing many more α variants and thus a weaker texture. In Ti64, strong crystallographic texture led to anisotropic mechanical properties and particularly influenced the fatigue performance [46–49]. A higher magnification SEM image of transformation microstructure at the β grain boundary in both builds are presented in Fig. 6. The majority of α_{GB} in the oscillation build are decorated with large α colonies oriented in one direction, indicating a strong crystallographic texture along the α_{GB}. Whereas the parallel pass build showed fine α colonies that are randomly oriented with weaker texture. In horizontal samples, the α_{GB} is perpendicular to the fatigue loading, where the majority of the single variant large α colonies are under fatigue loading and greatly influence the crack initiation, thereby fatigue life [28]. Hence fatigue property anisotropy is found. On the other hand, the weaker texture along the α_{GB} in parallel pass horizontal samples might not have influenced the fatigue life. Therefore, fatigue property anisotropy was not found. Further detail investigation of the role of microstructure and crystallographic texture along the α_{GB} is required to explain the anisotropy seen between the horizontal and vertical oscillation build samples, and this will be the subject of a future publication.

The relationships between fatigue strength and yield strength or

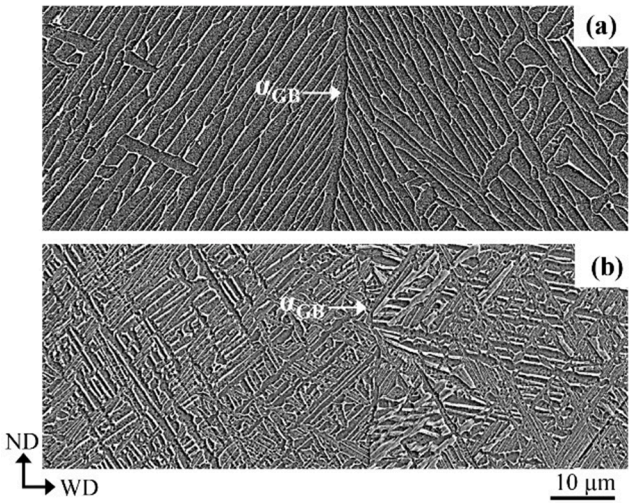

Fig. 6. SEM secondary electron (SE) high magnification images of the typical transformation microstructure at α_{GB} for oscillation (a) and parallel pass build (b).

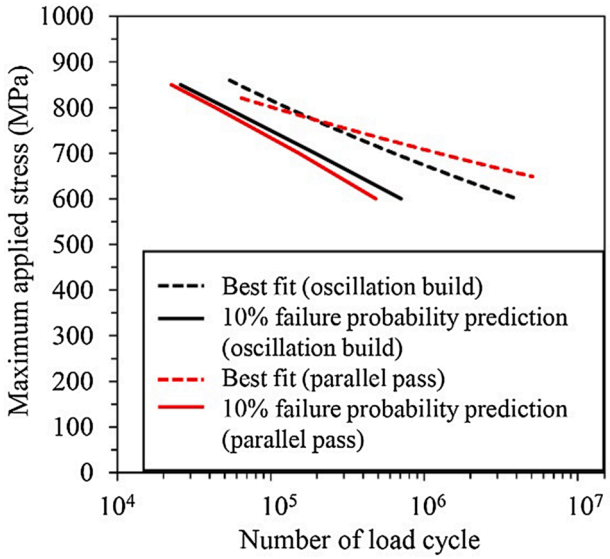

Fig. 7. Best fit curves of actual fatigue data and predicted S-N behaviour for a 10% probability failure. Runout samples were not considered in the 10% probability failure calculations.

hardness have been of interest where a single variable can be used to predict the fatigue limit of the material [50]. Because fatigue crack initiation is mainly caused by cyclic slip within grains, the yield strength or hardness has a correlation with the fatigue limit. In an ideal situation (i.e., no defects or small and isolated pores), one could estimate AM materials' fatigue strength by empirical equations. Murakami and Endo [50,51] proposed an empirical relation between the fatigue limit (σ_w) and the Vickers hardness (HV) when HV~400. The empirical formula between the σ_w and HV is given by Eq. (1)

$$\sigma_w = 1.6\text{HV} \pm 0.1\text{HV} \quad (1)$$

The equation (1) was initially developed for conventionally built steel alloys. Now it has already been applied to AM materials to predict the fatigue limit [52–55]. In this study, the Vickers hardness was measured for both the build strategies by using 0.5 kgf load applied for 10 seconds. For each sample, ten hardness measurements were made, finding average hardness value of 336 ± 4 for oscillation build and 350 ± 8 for parallel pass build. Using the hardness values and Eq. (1), predicted fatigue strength for oscillation and parallel pass builds was estimated as 538 ± 33 MPa and 560 ± 35 MPa. The estimated values are very close to the experimental values where the average (of the horizontal and vertical sample) fatigue strength of oscillation and parallel build is 550 MPa and 600 MPa, respectively.

From Figs. 4 and 5, it is apparent that there is a considerable scatter in the fatigue data for both the build strategies. The reasons for this will be discussed in the next section. Fatigue life scatters generally observed as the test samples and testing conditions are never identical. Consequently, a better representation of the fatigue data is required when using them to establish the required relationship for part/component design. In the presence of fatigue life scatter, the fatigue life curves can be better presented by the statistical analysis methods outlined in BS ISO 12,107 standard [56]. Figs. 4 and 5 show that the oscillation build showed very low fatigue property anisotropy, whereas no anisotropy is found in parallel pass deposit. The anisotropy in the oscillation build is very low and might have been influenced by the local microstructre and texture variation as discussed above. Therefore, we can consider that the oscillation build also has virtually isotropic fatigue properties. As both build methods are deemed to have isotropic failure properties, 10% failure probability was predicted in two build methods by combining both the sample orientation fatigue data using the procedure outlined in [56]. Predicted 10% failure probability at a 95% confidence level, and the best curves are presented in Fig. 7. Although the best fit curve showed marginally better fatigue performance in parallel pass build, a different trend is observed when 10% failure probability was estimated. The oscillation build showed a marginally better fatigue performance at lower applied stress. It appears that the large scatter in the fatigue data is also influenced the 10% failure probability.

3.4. Crack initiation sources

Fracture surface analysis showed different crack initiation sources covering the two build strategies and two sample orientations, Fig. 8. Only fracture surfaces of randomly selected samples are presented in Fig. 8. However, similar crack initiation locations were found in two build strategies. Based on the source and location of crack initiation, the SEM images are grouped into four; i) no defect, where crack initiated from a microstructure feature on the sample surface or internal, Fig. 8a. ii) crack initiation from a surface pore, Fig. 8b, iii) crack initiation from a subsurface pore where the distance between the pore and the nearest free surface is less than four times of pore diameter, Fig. 8c, and iv) crack initiation from an embedded defect, Fig. 8d. Most cracks were initiated from subsurface or embedded pores. All the pores are spherical, predominantly attributed to entrapped gas. Although optimised process parameters were used, resulting in the highest density material, scattered and small-sized pores in WAAM Ti64 were also reported in [12,26,27]. Pore diameter in the oscillation build ranged between 20 –110 μm with an average value of 75 μm, and a range of 5–140 μm with average diameter of 70 μm was found in parallel pass build. The proximity of pores to the sample surface ranged between 90 μm − 2 mm for oscillation build samples and 30 μm − 1.8 mm for parallel pass build smaples. Overall, 20% of samples had crack initiation from a microstructure feature (no defect), 4% samples had crack initiation from a surface pore, 18% samples had crack initiation from the sub-surface pore, and 47% samples had crack initiation from embedded pores. The remaining samples were test runouts (did not fail at 10^7 cycles).

To understand the influence of pore size on the fatigue life, crack initiating pore diameter vs. the fatigue life is plotted in Fig. 9. In our previous study [27], we investigated the effect of purposely introduced porosity defects on the fatigue performance of oscillation build vertical samples and found the critical pore diameter being around 100 μm. Fatigue strength was reduced by 8% in samples with pore diameter smaller than 100 μm and by around 40% when pore diameter was larger than 100 μm [27]. Based on this, we have considered 100 μm pore diameter is critical for WAAM Ti64, and this critical defect size is indicated in Fig. 9. It can observe that the majority of crack initiating pore size is below the critical pore size (i.e. 100 μm). A reasonably good correlation was found between pore diameter and fatigue life for most of the samples. However, oscillation built vertical samples tested at 800 and 600 MPa with the crack initiating pore diameter below the critical size did not follow the trend of increased pore diameter causing fatigue life reduction. In our recent study [28], we have found that for the same crack initiating pore size, pore surrounding with strong pyramidal texture and smaller α laths resulted in higher fatigue life. Most of the crack initiating pores were below 100 μm. Such small pores may be the consequence of wire quality, and the S-N data could be considered as virtually intrinsic material property (same as those without pores). In addition to the porosity size, surrounding microstructure and crystallographic texture at the pore might have contributed to the fatigue life scatter.

One of the most widely used models for small defects was proposed by Murakami [50] where spherical pores can be treated as a planar crack where the square root of the projected area of the pore is considered as the crack length. The stress intensity factor range is calculated using Eq. (2):

$$\Delta K = \text{C} \times \Delta\sigma(\sqrt{\pi\sqrt{area}}) \quad (2)$$

where ΔK is the stress intensity factor range, $\Delta\sigma$ is the applied stress range, $\sqrt{area}$ is the Murakami's square root of the projected area of the pore, geometrical parameter C equals to 0.5 for internal defects, 0.65 for surface defects [50]. Fig. 10 shows the stress intensity factor range vs. the fatigue life. Value of the threshold stress intensity factor range for WAAM Ti64 is 4.6 MPa $m^{1/2}$ [27] and indicated in Fig. 10. It shows a good correlation between ΔK and fatigue life where an increase in ΔK caused decrease in fatigue life.

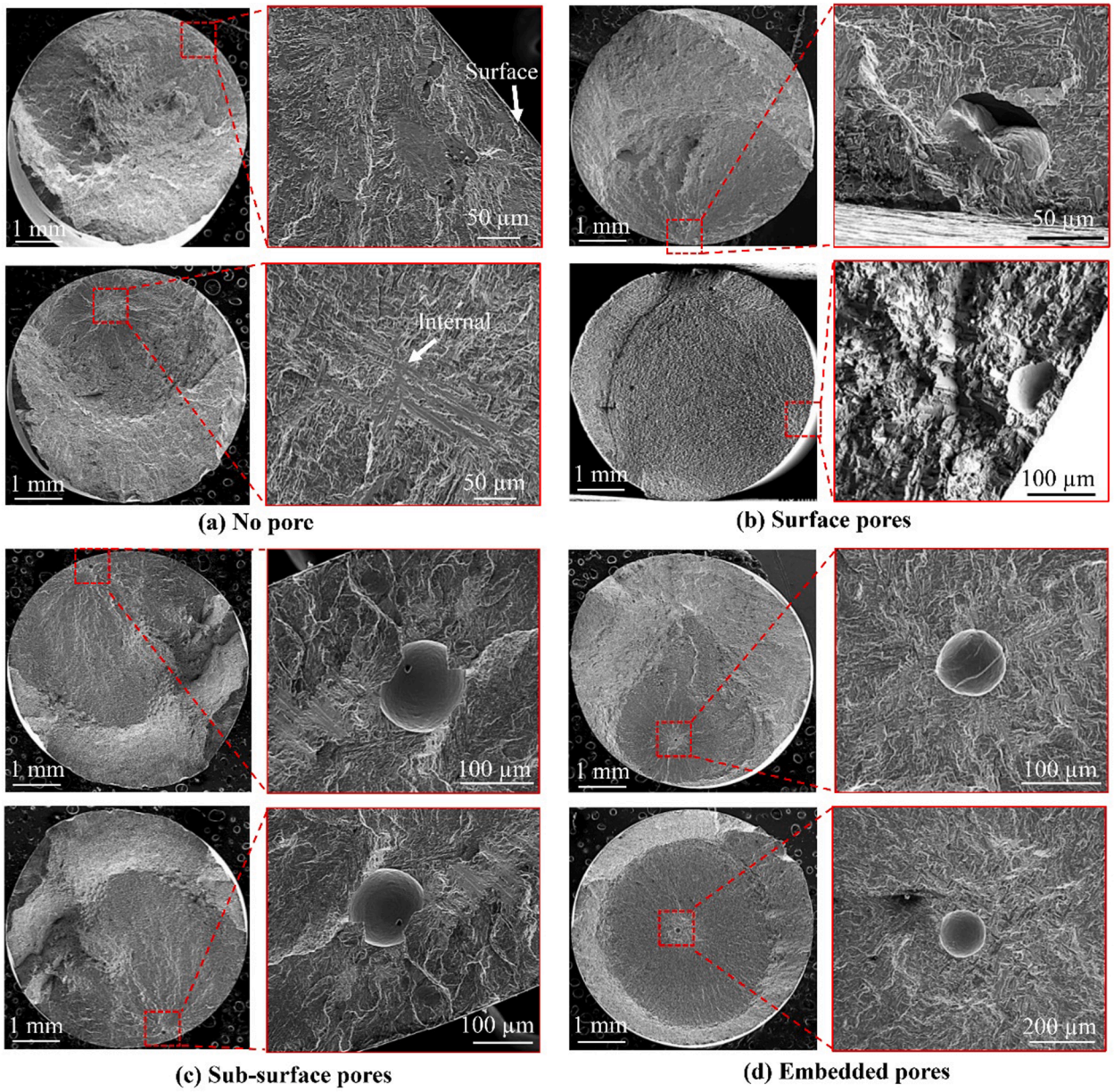

Fig. 8. SEM images of fracture surfaces (left) and crack initiation location of the corresponding sample in higher magnification (right).

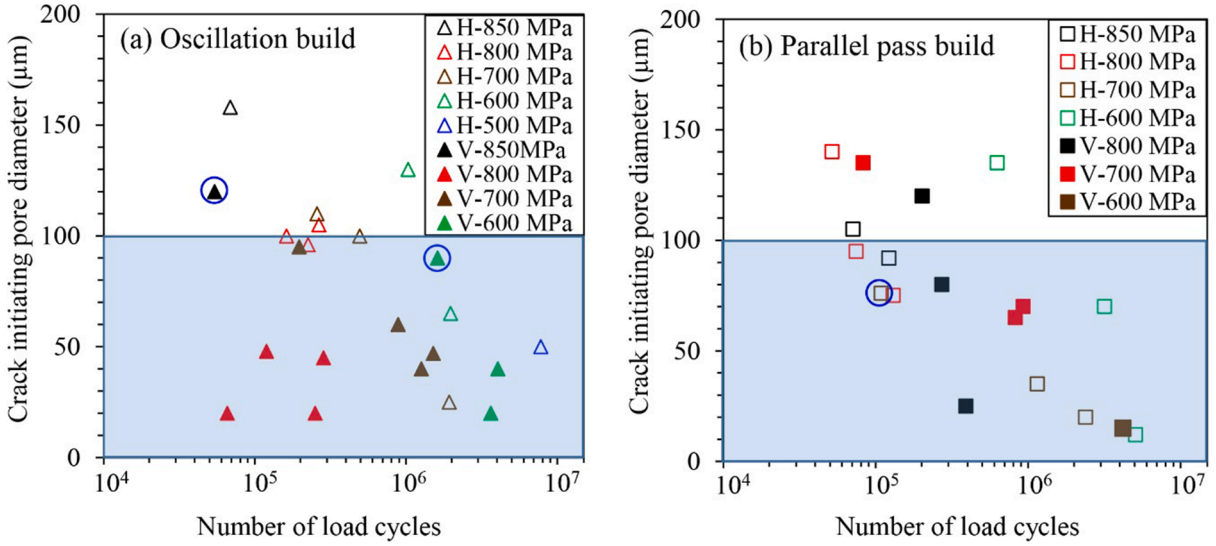

Fig. 9. Crack initiating pore diameter vs. fatigue life for oscillation and parallel pass builds. Encircled data points denote crack initiation at a surface pore. Runout samples are not included.

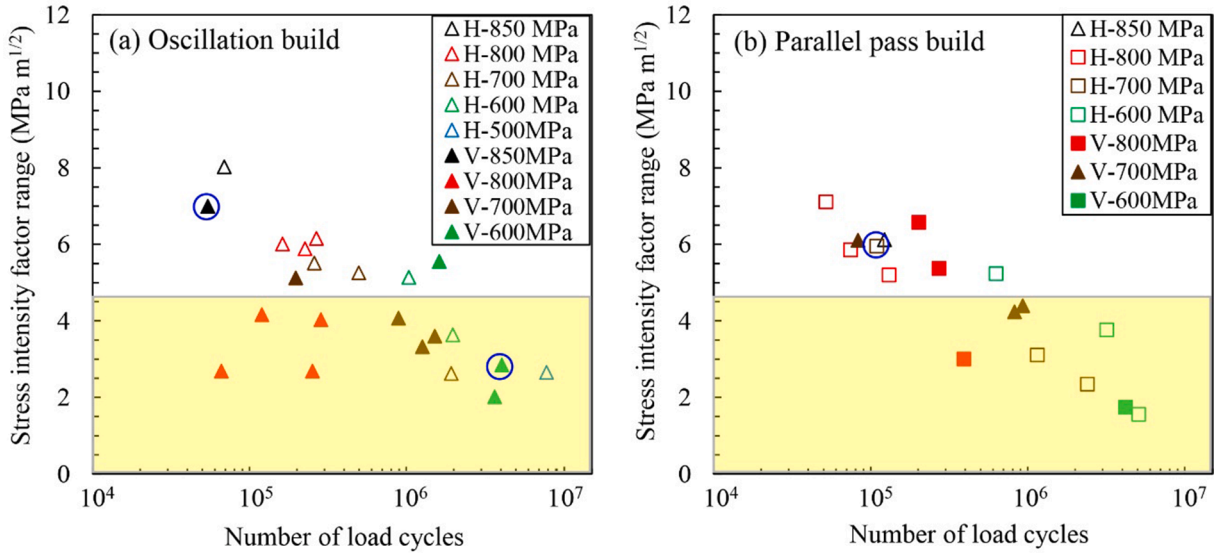

Fig. 10. Stress intensity factor range vs. fatigue life for (a) oscillation and (b) parallel pass builds. Encircled data points denote crack initiation at a surface pore. Runout samples are not included.

3.5. *Fracture mechanisms*

Fracture surfaces of tensile and fatigue specimens were analysed using SEM to study the fracture morphology. High magnification tensile fracture surfaces are presented in Fig. 11. The fractured surface profile of both builds exhibited deep dimples that indicate the ductile behaviour of the material. Oscillation build showed large dimples as a result of fracture along the large α colonies. Whereas smaller α width and α colonies resulted in smaller dimples formation in the parallel pass build.

Lower magnification SEM images showing fatigue fracture surface of oscillation and parallel pass build samples tested at 700 MPa are presented in Fig. 12. Both samples had crack initiation from a subsurface defect. Higher magnification images from three different regions within the same samples' fracture surface are also presented in Fig. 12. Three different fracture mechanisms can be observed. Region 1 shows the classic fatigue facets which were formed due to the cyclic slip process. The fracture facets are larger in the oscillation build indicated fracture along the large α colonies, whereas smaller α colonies in parallel pass build have smaller facets. Region 2 is the crack growth region which shows typical striation marks during the crack growth. Presence of striation marks in confined to smaller areas in the parallel pass build, whereas oscillation build showed longer striation marks. Finally, region

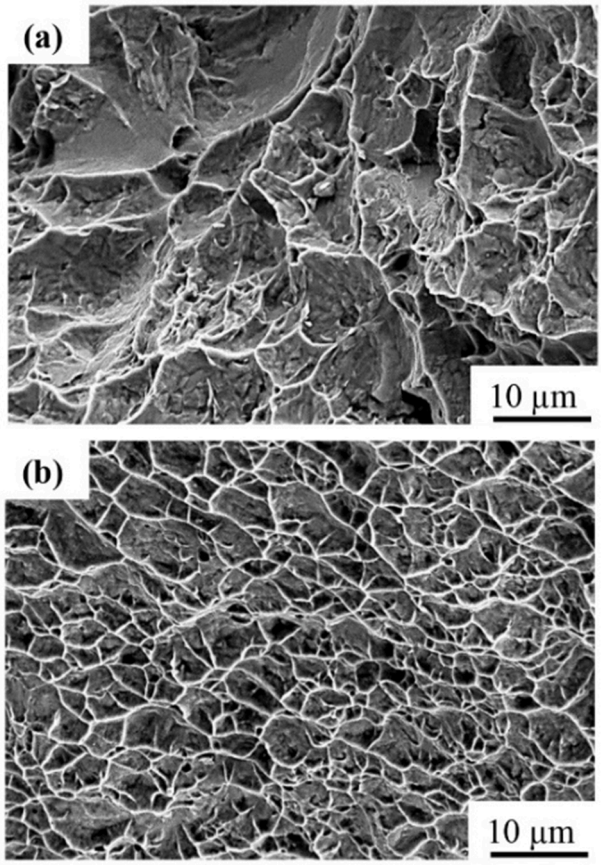

Fig. 11. Fracture surfaces of tensile test samples: (a) oscillation (b) parallel pass builds.

3 shows the final fracture. Oscillation build showed large ductile fracture dimples, like a tensile fracture, compared to parallel pass due to larger α colonies.

4. Conclusions

This paper presents a systematic study on the influence of oscillation and parallel pass deposition strategies in the WAAM process on the microstructure, tensile and high cycle fatigue properties of Ti-6Al-4V in the as-built condition. The key findings are:

1. Both build strategies resulted in columnar primary β grains aligned along the material build direction, a direct consequence of large thermal gradients and directional solidification. Higher heat inputs and slower cooling rates in the oscillation build resulted in wider columnar primary β grains and a coarser transformation α + β microstructure.
2. As a result of coarser transformation microstructure, oscillation build had lower yield and tensile strength compared to the parallel pass build. Columnar primary β grains resulted in 40% lower elongation in the horizontal samples compared to the vertical. This is due to the loading axis being normal to α_{GB} in the horizontal sample facilitating a preferential path for local damage accumulation along the grain boundary.
3. Fatigue strength at 10^7 cycles was 500 MPa for the oscillation build horizontal samples and 600 MPa for oscillation build vertical and both orientations in the parallel pass build. The finer transformation microstructure in the parallel pass build resulted in greater resistance to crack initiation, thereby higher fatigue limit than the oscillation build when comparing the horizontal samples
4. Small gas pores were the primary source of fatigue crack initiation and scatter in fatigue test data. Fractography revealed an average pore size of 70–75 μm in both build strategies. About 70% of samples failed due to crack initiation from small pores, and 20% of samples

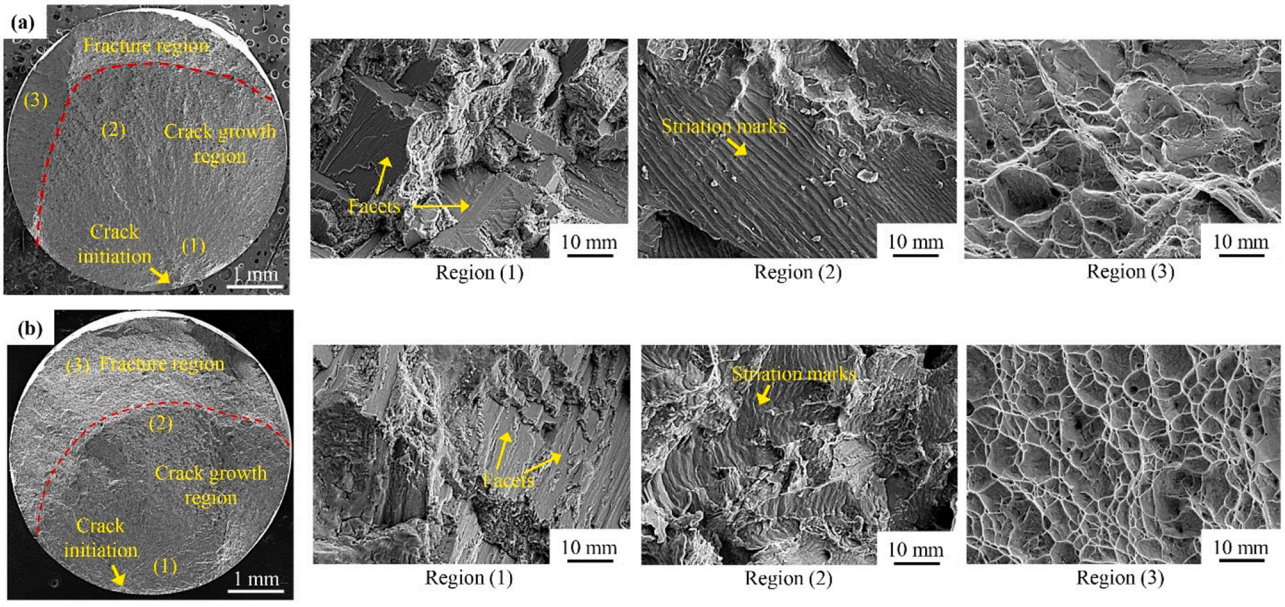

Fig. 12. Fatigue fracture surfaces showing different regions in (a) oscillation (b) parallel pass builds. Higher magnification images showing fracture surface features and fracture mechanism in different regions indicated in (a) and (b).

had crack initiation from a microstructure feature (i.e. no pores were found).

Declaration of Competing Interest

The authors declare that they have no known competing financial interests or personal relationships that could have appeared to influence the work reported in this paper.

Acknowledgements

The authors would like to thank Steve Damms and Barry Meek at Coventry University for their support on the sample machining, and the Engineering and Physical Sciences Research Council (EPSRC) for supporting this research through the NEWAM programme grant (EP/R027218/1).

Data availability

The raw/processed data required to reproduce these findings cannot be shared at this time as the data also forms part of an ongoing study.

References

[1] Frazier WE. Metal additive manufacturing: a review. J Mater Eng Perform 2014;23:1917–28. https://doi.org/10.1007/s11665-014-0958-z.
[2] Liu S, Shin YC. Additive manufacturing of Ti6Al4V alloy: a review. Mater Des 2019;164:107552. https://doi.org/10.1016/J.MATDES.2018.107552.
[3] DebRoy T, Wei HL, Zuback JS, Mukherjee T, Elmer JW, Milewski JO, et al. Additive manufacturing of metallic components – Process, structure and properties. Prog Mater Sci 2018;92:112–224. https://doi.org/10.1016/J.PMATSCI.2017.10.001.
[4] ASTM F2924-14, Standard Specification for Additive Manufacturing Titanium-6 Aluminum-4 Vanadium with Powder Bed Fusion, in: ASTM Int., West Conshohocken, PA; 2014.
[5] Qiu C, Adkins NJE, Attallah MM. Microstructure and tensile properties of selectively laser-melted and of HIPed laser-melted Ti-6Al-4V. Mater Sci Eng A. 2013;578:230–9. https://doi.org/10.1016/j.msea.2013.04.099.
[6] Rafi HK, Karthik NV, Gong H, Starr TL, Stucker BE. Microstructures and mechanical properties of Ti6Al4V parts fabricated by selective laser melting and electron beam melting. J Mater Eng Perform 2013;22:3872–83. https://doi.org/10.1007/s11665-013-0658-0.
[7] Vilaro T, Colin C, Bartout JD. As-fabricated and heat-treated microstructures of the Ti-6Al-4V alloy processed by selective laser melting. Metall Mater Trans A Phys Metall Mater Sci 2011;42:3190–9. https://doi.org/10.1007/s11661-011-0731-y.
[8] Körner C. Additive manufacturing of metallic components by selective electron beam melting - A review. Int Mater Rev 2016;61:361–77. https://doi.org/10.1080/09506608.2016.1176289.
[9] Alcisto J, Enriquez A, Garcia H, Hinkson S, Steelman T, Silverman E, et al. Tensile Properties and Microstructures of Laser-Formed Ti-6Al-4V. J Mater Eng Perform 2011;20:203–12. https://doi.org/10.1007/s11665-010-9670-9.
[10] Carroll BE, Palmer TA, Beese AM. Anisotropic tensile behavior of Ti-6Al-4V components fabricated with directed energy deposition additive manufacturing. Acta Mater 2015;87:309–20. https://doi.org/10.1016/j.actamat.2014.12.054.
[11] Williams SW, Martina F, Addison AC, Ding J, Pardal G, Colegrove P. Wire + Arc Additive Manufacturing. Mater Sci Technol 2016;32:641–7. https://doi.org/10.1179/1743284715Y.0000000073.
[12] Wang F, Williams S, Colegrove P, Antonysamy AA. Microstructure and mechanical properties of wire and arc additive manufactured Ti-6Al-4V. Metall Mater Trans A Phys Metall Mater Sci 2013;44:968–77. https://doi.org/10.1007/s11661-012-1444-6.
[13] Colegrove PA, Coules HE, Fairman J, Martina F, Kashoob T, Mamash H, et al. Microstructure and residual stress improvement in wire and arc additively manufactured parts through high-pressure rolling. J Mater Process Technol 2013;213:1782–91. https://doi.org/10.1016/j.jmatprotec.2013.04.012.
[14] Martina F, Colegrove PA, Williams SW, Meyer J. Microstructure of interpass rolled wire + arc additive manufacturing Ti-6Al-4V components. Metall Mater Trans A Phys Metall Mater Sci 2015;46:6103–18. https://doi.org/10.1007/s11661-015-3172-1.
[15] Donoghue J, Antonysamy AA, Martina F, Colegrove PA, Williams SW, Prangnell PB. The effectiveness of combining rolling deformation with wire–arc additive manufacture on β-grain refinement and texture modification in Ti–6Al–4V. Mater Charact 2016;114:103–14. https://doi.org/10.1016/j.matchar.2016.02.001.
[16] McAndrew AR, Alvarez Rosales M, Colegrove PA, Hönnige JR, Ho A, Fayolle R, et al. Interpass rolling of Ti-6Al-4V wire + arc additively manufactured features for microstructural refinement. Addit Manuf 2018;21:340–9. https://doi.org/10.1016/J.ADDMA.2018.03.006.
[17] Hönnige JR, Colegrove P, Williams S. Improvement of microstructure and mechanical properties in wire + arc additively manufactured Ti-6Al-4V with machine hammer peening. Proc Eng 2017;216:8–17. https://doi.org/10.1016/j.proeng.2018.02.083.
[18] Neto L, Williams S, Ding J, Hönnige J, Martina F. Mechanical properties enhancement of additive manufactured Ti-6Al-4V by machine hammer peening. In: Itoh S, Shukla S, editors. Adv. Springer Singapore, Singapore: Surf. Enhanc; 2020. p. 121–32.
[19] F. Martina, S.. Williams, P. Colegrove, Improved microstructure and increased mechanical properties of additive manufacture produced TI-6AL-4V by interpass cold rolling, in: 24th Int. Solid Free. Fabr. Symp. - An Addit. Manuf. Conf., Austin, United States, 2013: pp. 490–496.
[20] Metallic Materials Properties Development and Standardization (MMPDS-04), 2008.
[21] Yi H-J, Kim J-W, Kim Y-L, Shin S. Effects of cooling rate on the microstructure and tensile properties of wire+arc additive manufactured Ti–6Al–4V alloy. Met Mater Int 2020;26:1235–46. https://doi.org/10.1007/s12540-019-00563-1.
[22] Wu B, Pan Z, Ding D, Cuiuri D, Li H, Fei Z. The effects of forced interpass cooling on the material properties of wire arc additively manufactured Ti6Al4V alloy. J Mater Process Technol 2018;258:97–105. https://doi.org/10.1016/j.jmatprotec.2018.03.024.
[23] Ding D, Wu B, Pan Z, Qiu Z, Li H. Wire arc additive manufacturing of Ti6Al4V using active interpass cooling. Mater Manuf Process 2020;35:845–51. https://doi.org/10.1080/10426914.2020.1732414.
[24] Bermingham MJ, Nicastro L, Kent D, Chen Y, Dargusch MS. Optimising the mechanical properties of Ti-6Al-4V components produced by wire + arc additive manufacturing with post-process heat treatments. J Alloys Compd 2018;753:247–55. https://doi.org/10.1016/j.jallcom.2018.04.158.
[25] Bermingham MJ, Kent D, Zhan H, Stjohn DH, Dargusch MS. Controlling the microstructure and properties of wire arc additive manufactured Ti-6Al-4V with trace boron additions. Acta Mater 2015;91:289–303. https://doi.org/10.1016/j.actamat.2015.03.035.
[26] Biswal R, Zhang X, Shamir M, Al Mamun A, Awd M, Walther F, et al. Interrupted fatigue testing with periodic tomography to monitor porosity defects in wire + arc additive manufactured Ti-6Al-4V. Addit. Manuf. 2019;28:517–27. https://doi.org/10.1016/J.addma.2019.04.026.
[27] Biswal R, Zhang X, Syed AK, Awd M, Ding J, Walther F, et al. Criticality of porosity defects on the fatigue performance of wire + arc additive manufactured titanium alloy. Int J Fatigue. 2019;122:208–17. https://doi.org/10.1016/J.ijfatigue.2019.01.017.
[28] Shamir M, Syed AK, Janik V, Biswal R, Zhang X. The role of microstructure and local crystallographic orientation near porosity defects on the high cycle fatigue life of an additive manufactured Ti-6Al-4V. Mater Charact 2020;169:110576. https://doi.org/10.1016/j.matchar.2020.110576.
[29] Lockett H, Ding J, Williams S, Martina F. Design for Wire + Arc Additive Manufacture: design rules and build orientation selection. J Eng Des 2017;28:568–98. https://doi.org/10.1080/09544828.2017.1365826.
[30] Bandari Y, Charrett T, Michel F, Ding J, Williams S, Tatum RP. Compensation strategies for robotic motion errors for additive manufacturing (AM). in 2016.
[31] ASTM E8 / E8M-16ae1, standard test methods for tension testing of metallic materials, in: ASTM Int., West Conshohocken, PA, 2016.
[32] ASTM E466-15, standard practice for conducting force controlled constant amplitude axial fatigue tests of metallic materials, in: ASTM Int., West Conshohocken, PA, 2015. doi:10.1520/E0466-15.2.
[33] ASTM E1382-97, standard test methods for determining average grain size using semiautomatic and automatic image analysis, in: ASTM Int., West Conshohocken, PA, 2015.
[34] Ho A, Zhao H, Fellowes JW, Martina F, Davis AE, Prangnell PB. On the origin of microstructural banding in Ti-6Al4V wire-arc based high deposition rate additive manufacturing. Acta Mater 2019;166:306–23. https://doi.org/10.1016/J.actamat.2018.12.038.
[35] Kobryn P, Semiatin S. Microstructure and texture evolution during solidification processing of Ti–6Al–4V. J Mater Process Technol 2003;135:330–9. https://doi.org/10.1016/S0924-0136(02)00865-8.
[36] Kelly SM, Kampe SL. Microstructural evolution in laser-deposited multilayer Ti-6Al-4V builds: Part I. Microstructural characterization. Metall Mater Trans A. 2004;35:1861–7. https://doi.org/10.1007/s11661-004-0094-8.
[37] Baufeld B, Brandl E, Van Der Biest O. Wire based additive layer manufacturing: comparison of microstructure and mechanical properties of Ti-6Al-4V components fabricated by laser-beam deposition and shaped metal deposition. J Mater Process Technol 2011;211:1146–58. https://doi.org/10.1016/j.jmatprotec.2011.01.018.
[38] Al-Bermani SS, Blackmore ML, Zhang W, Todd I. The origin of microstructural diversity, texture, and mechanical properties in electron beam melted Ti-6Al-4V. Metall. Mater. Trans. A Phys. Metall. Mater. Sci. 2010;41:3422–34. https://doi.org/10.1007/s11661-010-0397-x.
[39] Antonysamy AA, Meyer J, Prangnell PB. Effect of build geometry on the β-grain structure and texture in additive manufacture of Ti6Al4V by selective electron beam melting. Mater. Charact. 2013;84:153–68. https://doi.org/10.1016/j.matchar.2013.07.012.
[40] Colegrove PA, Donoghue J, Martina F, Gu J, Prangnell P, Hönnige J. Application of bulk deformation methods for microstructural and material property improvement and residual stress and distortion control in additively manufactured components. Scr. Mater. 2016;2. https://doi.org/10.1016/j.scriptamat.2016.10.031.
[41] Lütjering G. Property optimization through microstructural control in titanium and aluminum alloys. Mater. Sci. Eng. A. 1999;263:117–26. https://doi.org/10.1016/S0921-5093(98)01169-1.

[42] Lütjering G. Influence of processing on microstructure and mechanical properties of (α+β) titanium alloys. Mater. Sci. Eng. A. 1998;243:32–45. https://doi.org/10.1016/S0921-5093(97)00778-8.
[43] Wu GQ, Shi CL, Sha W, Sha AX, Jiang HR. Effect of microstructure on the fatigue properties of Ti–6Al–4V titanium alloys. Mater. Des. 2013;46:668–74. https://doi.org/10.1016/J.matdes.2012.10.059.
[44] Donachie MJ. Titanium, A technical guide. 2nd edition. Metals Park (OH): ASM International; 2000.
[45] Lütjering G, Williams J. Titanium. Berlin Heidelberg: Springer-Verlag; 2007.
[46] Peters M, Gysler A, Lütjering G. Influence of texture on fatigue properties of Ti-6Al-4V. Metall. Mater. Trans. A. 1984;15:1597–605. https://doi.org/10.1007/BF02657799.
[47] Pilchak AL, Williams REA, Williams JC. Crystallography of fatigue crack initiation and growth in fully lamellar Ti-6Al-4V. Metall. Mater. Trans. A. 2010;41:106–24. https://doi.org/10.1007/s11661-009-0064-2.
[48] Le Biavant K, Pommier S, Prioul C. Local texture and fatigue crack initiation in a Ti-6Al-4V titanium alloy. Fatigue Fract. Eng. Mater. Struct. 2002;25:527–45. https://doi.org/10.1046/j.1460-2695.2002.00480.x.
[49] Kocks UF, Tomé CN, Wenk HR. Texture and Anisotropy: Preferred Orientations in Polycrystals and Their Effect on Materials Properties. Cambridge: Cambridge University Press; 2000.
[50] Murakami Y. Metal Fatigue: effects of small defects and nonmetallic inclusions. First edit: Elsevier; 2002.
[51] Murakami Y, Endo M. Effects of hardness and crack geometry on ΔKth of small cracks. Mater. Sci. 1986;275–293.
[52] Yamashita Y, Murakami T, Mihara R, Okada M, Murakami Y. Defect analysis and fatigue design basis for Ni-based superalloy 718 manufactured by selective laser melting. Int. J. Fatigue. 2018;117:485–95. https://doi.org/10.1016/j.ijfatigue.2018.08.002.
[53] Gunther J, Krewerth D, Lippmann T, Leuders S, Troster T, Weidner A, et al. Fatigue life of additively manufactured Ti-6Al-4V in the very high cycle fatigue regime. Int. J. Fatigue. 2017;94:236–45. https://doi.org/10.1016/j.ijfatigue.2016.05.018.
[54] Masuo H, Tanaka Y, Morokoshi S, Yagura H, Uchida T, Yamamoto Y, et al. Effects of Defects, Surface Roughness and HIP on Fatigue Strength of Ti-6Al-4V manufactured by Additive Manufacturing. Proc Struct Integr 2017;7:19–26. https://doi.org/10.1016/j.prostr.2017.11.055.
[55] Kakiuchi T, Kawaguchi R, Nakajima M, Hojo M, Fujimoto K, Uematsu Y. Prediction of fatigue limit in additively manufactured Ti-6Al-4V alloy at elevated temperature. Int. J. Fatigue. 2019;126:55–61. https://doi.org/10.1016/j.ijfatigue.2019.04.025.
[56] BS ISO. 12107 standard for metallic materials-fatigue testing-statistical planning and analysis of data, in. Br. Stand., British Standards Institution 2003.

https://dspace.org/

Influence of deposition strategies on tensile and fatigue properties in a wire + arc additive manufactured Ti-6Al-4V

Syed, Abdul Khadar; Zhang, Xiang; Caballero, Armando; Shamir, Muhammad; Williams, Stewart

2021-04-15
Elsevier
https://doi.org/10.1016/j.ijfatigue.2021.106268
Syed AK, Zhang X, Caballero A, et al., (2021) Influence of deposition strategies on tensile and fatigue properties in a wire + arc additive manufactured Ti-6Al-4V. International Journal of Fatigue, Volume 149, August 2021, Article number 106268

Downloaded from a DSpace repository. https://dspace.org/